

**Modifications to WRF's dynamical core to improve the
treatment of moisture for large-eddy simulations**

Heng Xiao¹, Satoshi Endo², May Wong¹, William C. Skamarock³, Joseph B. Klemp³, Jerome D.
Fast¹, William I. Gustafson Jr.¹, Andrew M. Vogelmann², Hailong Wang¹, Yangang Liu², and
Wuyin Lin²

¹ Atmospheric Science and Global Change Division, Pacific Northwest National Laboratory

² Brookhaven National Laboratory

³ National Center for Atmospheric Research

September 28, 2015

Revised for *Journal of Advances in Modeling Earth Systems*

Abstract

Yamaguchi and Feingold (2012) note that the cloud fields in their large-eddy simulations (LESs) of marine stratocumulus using the Weather Research and Forecasting (WRF) model exhibit a strong sensitivity to time stepping choices. In this study, we reproduce and analyze this sensitivity issue using two stratocumulus cases, one marine and one continental. Results show that (1) the sensitivity is associated with spurious motions near the moisture jump between the boundary layer and the free atmosphere, and (2) these spurious motions appear to arise from neglecting small variations in water vapor mixing ratio (q_v) in the pressure gradient calculation in the acoustic sub-stepping portion of the integration procedure. We show that this issue is remedied in the WRF dynamical core by replacing the prognostic equation for the potential temperature θ with one for the moist potential temperature $\theta_m = \theta(1 + 1.61q_v)$, which allows consistent treatment of moisture in the calculation of pressure during the acoustic sub-steps. With this modification, the spurious motions and the sensitivity to the time stepping settings (i.e., the dynamic time step length and number of acoustic sub-steps) are eliminated in both of the example stratocumulus cases. This modification improves the applicability of WRF for LES applications, and possibly other models using similar dynamical core formulations, and also permits the use of longer time steps than in the original code.

1. Introduction

The Weather Research and Forecasting (WRF) model [Skamarock et al., 2008] is a mesoscale numerical weather model designed for atmospheric research and operational forecasting. In recent years, WRF has gained popularity as a large-eddy simulation (LES) model due to its built-in nesting capability, its open and modularized structure that facilitates the implementation of new physical parameterizations, and its fully compressible nonhydrostatic dynamic core [e.g., Moeng et al. 2007; Wang et al. 2009; Wang and Feingold 2009a, b; Yamaguchi and Feingold 2012; Blossey et al. 2013; Yamaguchi et al. 2013; Xiao et al. 2014; Endo et al. 2015].

Yamaguchi and Feingold [2012] (hereafter YF12) performed LESs using WRF v3.3.1 for two stratocumulus cases developed by the boundary layer cloud working group of the Global Energy and Water Cycle Experiment (GEWEX) Cloud System Study (GCSS; currently, Global Atmospheric System Studies (GASS)) panel. The cases are based on the first and second research flights (RF01 and RF02) of the Second Dynamics and Chemistry of Marine Stratocumulus field study (DYCOMS-II) field campaign [Stevens et al. 2003; Stevens et al. 2005; Ackerman et al. 2009]. YF12 showed that the simulated stratocumulus cloud fraction and liquid water path (LWP) depend sensitively on the choice of the dynamic integration time step (Δt) and the number of acoustic sub-steps (N_{aco}) used in each time step (see their Figure 5); this dependence is hereafter referred to as the convergence issue. For example, they found that in the DYCOMS-II RF01 case the simulated LWP shows evidence of convergence only when Δt is reduced to 0.1 s and N_{aco} is increased to 10 or 12. These time-stepping choices lead to acoustic Courant numbers far smaller than those required by the Courant-Friedrichs-Lewy (CFL) criterion. Based on this criterion, YF12 should have been able to use $\Delta t=0.2$ s and $N_{aco} \geq 4$ for their 35 m horizontal grid spacing. They concluded by advising “a convergence test be performed every time the model configuration is changed,” which can be a tedious and computationally expensive requirement for LES applications.

In this study, we identify the cause of this convergence issue and present a solution for WRF. In Section 2, the issue is demonstrated for one of the aforementioned marine stratocumulus cases (the DYCOMS-II RF02 case) and a continental stratocumulus case. Evidence is provided showing that this convergence issue arises from spurious motions

occurring at levels with large vertical moisture gradients, e.g., at the trade wind inversion in the DYCOMS-II cases. Section 3 demonstrates that these spurious motions are due to the omission of the effect of small moisture perturbations on the pressure perturbations during the acoustic sub-step integration as formulated in the current WRF model. A modification to WRF’s dynamical core is presented in Section 4, which allows consistent treatment of moisture in the calculation of pressure during the acoustic sub-steps, along with demonstration that this modification eliminates the spurious motions and resolves the convergence issue. Finally, a summary of the findings is presented in Section 5.

2. The convergence issue and spurious motions near the inversion

2.1 DYCOMS-II RF02 case

We first explore the convergence issue using the DYCOMS-II RF02 marine stratocumulus case, one of the cases examined in YF12, which represents nocturnal stratocumulus clouds in a quasi-steady marine boundary layer capped by a strong inversion. The case derives from the RF02 flight during the DYCOMS-II field campaign conducted off the coast of California during July 2001 [Stevens et al. 2003; Ackerman et al. 2009].

For this case we use WRF 3.6.1 and configure the model following the original case specification by Ackerman et al. [2009]. The model domain is $6.4 \text{ km} \times 6.4 \text{ km} \times 1.5 \text{ km}$ with 50 m horizontal grid spacing and 96 vertical layers. The vertical grid is stretched such that the grid spacing near the surface and inversion, with a minimum of 5 m, is smaller than the grid spacing in the middle of the boundary layer or in the free atmosphere. We use the simple longwave radiation scheme following Stevens et al. [2005] and the Lin microphysics scheme [Lin et al. 1983] modified to include cloud water sedimentation following Ackerman et al. [2009]. Surface fluxes and large-scale subsidence are also prescribed following Ackerman et al. [2009]. Figure 1 shows the initial profiles for the DYCOMS-II RF02 case.

The results from simulations with $\Delta t = 0.5 \text{ s}$ and various N_{aco} settings are given in Figure 2, which shows time series of LWP, cloud-base and cloud-top heights, and total cloud fraction. The ensemble mean and spread from the LES simulations reported in

Ackerman et al. [2009] are also shown for comparison. The results for simulations with $N_{aco} = 10$ and 12 are in close agreement for all four cloud variables, indicating a converged solution, which lies within the ensemble range from Ackerman et al. [2009]; however, the simulation with $N_{aco} = 6$ is markedly different, particularly in terms of LWP and total cloud fraction, indicating non-convergence. The cloud fraction and LWP for $N_{aco} = 8$ are slightly lower than those for $N_{aco} = 10$ and 12. Thus, these simulations reproduce in a newer WRF version the convergence issue (or acoustic time-step dependency) raised by YF12 for the DYCOMS-II RF02 case.

Vertical profiles of meteorological variables from the simulations using different N_{aco} are depicted in Figure 3. Similar to the time-series results, the simulation using $N_{aco} = 6$ clearly diverges from the other simulations. Compared to the converged simulations, the $N_{aco} = 6$ simulation has smoother vertical variations in potential temperature, water vapor mixing ratio, and horizontal winds across the inversion, and smaller liquid water mixing ratio and cloud fraction near the inversion. The profiles of turbulence characteristics, such as variances and covariances, also have differences around the inversion and in the cloud layer (not shown). Both the time series and vertical profiles show convergence of the cloud variables in the simulations using $N_{aco} \geq 10$; thus, for the following discussion, we focus on $N_{aco} = 12$ and 6, representing the converged and non-converged solutions, respectively.

To better understand the processes leading to non-convergence, one needs to examine conditions when the non-converged and converged simulations start to diverge. Figure 4 shows the vertical cross sections of perturbations of zonal wind, vertical velocity, water vapor mixing ratio, and water vapor tendency due to condensation/evaporation 30 minutes into the simulation for $N_{aco} = 6$ and $N_{aco} = 12$. The perturbation is defined as the deviation from the horizontal average; e.g., for zonal wind u , the perturbation $u' = u - \bar{u}$, where \bar{u} is the horizontal average. The $N_{aco} = 6$ simulation shows spurious motions near the inversion for all four variables, which do not appear in the $N_{aco} = 12$ simulation. These spurious motions are consistent with the smoother profiles in the $N_{aco} = 6$ simulation (Figure 3). They reflect stronger mixing across the inversion to which the stratocumulus clouds are very sensitive, as can be seen from the water vapor tendency due to condensation/evaporation. It seems likely that the difference between the $N_{aco} = 12$ and

$N_{aco} = 6$ simulations in terms of cloud fraction, LWP, and cloud layer thickness, are caused by these spurious motions. Interestingly, these spurious motions seem to grow slowly, over minutes to tens of minutes compared to error growth that grows over several time steps when violating CFL conditions, and the spurious motions saturate as the inversion gets mixed out and becomes smoother during the integration (not shown).

Numerous sensitivity simulations are performed to identify conditions associated with the convergence issue and the spurious motions near the inversion. The convergence issue, as measured by the differences in cloud fraction and LWP between the $N_{aco} = 12$ and $N_{aco} = 6$ simulations, and the magnitude of the spurious motions depend strongly on two factors: horizontal wind speed and the moisture jump Δq_v across the inversion.

The impact of the first factor is shown by modifying the initial horizontal winds in three sensitivity tests such that both the zonal and meridional winds are either (1) zero at all levels, (2) constant in height but nonzero, i.e., with no wind shear, or (3) zero at the inversion height but with a constant nonzero wind shear. In (2) the winds at the inversion level in the control run are applied throughout the vertical domain while in (3) the wind shear at the inversion level in the control run is applied throughout the depth of the model domain. The modified wind profiles can be seen in Figure 1. The sensitivities to initial wind conditions are shown in Figure 5. For the “no initial wind” and the “zero wind speed at inversion” simulations, the results using $N_{aco} = 6$ and 12 are in close agreement. However, for the “no wind shear” simulations, the difference between the two simulations is even slightly larger than in the control set of simulations. Therefore, we conclude that wind speed at the inversion height, but not wind shear, can cause the lack of convergence in the DYCOMS-II RF02 case. Interestingly, although wind shear is generally considered to be an important factor for cloud-top entrainment that contributes to cloud dissipation, shear is not a controlling factor for the convergence issue.

To test the impact of the second factor, we modify the magnitude of the initial moisture jump at the inversion height as shown in Figure 1. The DYCOMS-II RF02 case uses a simple step function of total water mixing ratio to define the moisture jump at the inversion that can be written as $\Delta q_v = q_{bot} - q_{top}$, where q_{top} is the water vapor mixing ratio at the top of the inversion (5 g kg⁻¹ for the control simulation) and q_{bot} is that at the bottom

of the inversion (8.6 g kg^{-1}) resulting in $\Delta q_v = 3.6 \text{ g kg}^{-1}$ for the control. The magnitude of the moisture jump in the sensitivity tests is reduced by 1 and 2 g kg^{-1} by setting $q_{top} = 6$ and 7 g kg^{-1} , respectively. The sensitivity of LWP to changes in the magnitude of the moisture jump is shown in Figure 6. When the moisture jump is reduced by 1 g kg^{-1} , the divergence in LWP between the $N_{aco}=12$ and $N_{aco}=6$ simulations is significantly reduced. When the moisture jump is reduced by 2 g kg^{-1} , the two simulations appear to converge. Sensitivity tests using even larger reductions in the moisture jump also show convergence for smaller values of N_{aco} (not shown).

In both sets of sensitivity tests, when LWP in the $N_{aco}=6$ simulation converges to the value in the corresponding $N_{aco}=12$ simulation, the spurious motions near the inversion disappear. This further confirms that the spurious motions are responsible for the divergence of simulations with different N_{aco} .

2.2 ARM SGP stratocumulus case

A second case with stratocumulus clouds over land serves to demonstrate the generality of the issue, which has not been previously shown. On 13 May 2008, a very strong temperature inversion and moisture jump occurred at the U.S. Department of Energy (DOE) Atmospheric Radiation Measurement (ARM) Program Climate Research Facility (CRF) at the Southern Great Plains (SGP) site (hereafter referred to as the ARM SGP site) for the early-morning profiles of potential temperature, water vapor mixing ratio, and horizontal winds at 1130 UTC (0530 LST) as shown in Figure 7. The water vapor mixing ratio jumps from $\sim 1 \text{ g kg}^{-1}$ at $\sim 1.6 \text{ km}$ to $\sim 13 \text{ g kg}^{-1}$ at $\sim 1.2 \text{ km}$. The profiles of potential temperature and horizontal winds also show a very distinct two-layer structure below 5 km. This radiosonde profile has a much stronger moisture jump across the inversion and stronger winds compared to the previous case (Figure 1), providing a very stringent test for the convergence issue.

For this case, we use WRF version 3.6.1 with the Morrison double-moment microphysics [Morrison et al. 2009] and RRTMG radiation schemes [Iacono et al. 2008]. It will be shown later that the convergence issue and its solution do not depend on the choice of physical parameterizations. Subgrid-scale (SGS) turbulent mixing is parameterized using

the 1.5-order TKE closure based on Deardorff [1980]. Surface latent and sensible heat fluxes are prescribed from the ARM Best Estimates (ARMBE) dataset [ARM CRF, 1994; Xie et al. 2010]. Surface roughness length is set to 0.04 m, surface albedo to 0.2, and emissivity to 1.0 following Endo et al. [2015] based on their case from the Routine ARM Aerial Facility (AAF) Clouds with Low Optical Water Depths (CLOWD) Optical Radiative Observations (RACORO) campaign. No large-scale advective tendencies of temperature and moisture are applied for this case. The simulations start at 1200 UTC and are integrated for 15 hours. Random initial perturbations to the temperature profile shown in Figure 7 are applied in the lowest 5 model layers. Model grid spacing is 100 m in the horizontal and ~ 20 m in the vertical, and the model domain is 25.6 km by 25.6 km in the horizontal and 5 km in the vertical with a 500 m deep sponge layer at the model top. We present four simulations that differ only by their time steps ($\Delta t=0.5$ and 1.0 s) and acoustic sub-steps ($N_{aco}=6$ and 12).

Figure 8 shows the evolution of LWP and total cloud cover for the four simulations. Total cloud cover from the Total Sky Imager (TSI; [ARM CRF, 2000]) and LWP from the Microwave Radiometer Retrievals (MWRRET; [ARM CRF, 1996; Turner et al., 2007]) at the ARM SGP site are shown for comparison. Some of the quantitative differences in terms of cloud fraction are due to observed cirrus (seen in TSI images) at different times during the simulation period, which are above the model top. Two primary discrepancies exist between the simulations and reality. Unlike the observations, the model produces no cloud during the first two simulated hours. And, the observed secondary peak in LWP and cloud cover around 1600 LST is absent in the simulations. We believe these two discrepancies are associated with either our simple initialization or the neglect of large-scale advective forcing. Fortunately, for our present purposes the lack of clouds in the morning allows us to examine the model behavior in clear-sky conditions, i.e., before the cloud microphysics parameterization is active.

The convergence issue is produced in this case as well: the peak LWP value around 0930 LST drops from 97 g m^{-2} with $\Delta t=0.5$ s and $N_{aco}=12$, to 20 g m^{-2} with $\Delta t=1.0$ s and $N_{aco}=6$, and peak cloud fraction drops from 1.0 to 0.8. As Figure 9 shows, the strength of the spurious motions near the inversion also decreases with decreasing Δt and increasing N_{aco} , consistent with the increasing LWP. The spurious signal becomes negligible compared to

near-surface perturbations only when $\Delta t=0.25$ s and $N_{aco}=12$ (not shown). We found that for this SGP test case, the same sensitivity exists as in the DYCOMS-II RF02 case regarding the dependence of the spurious motions on the moisture jump and wind speed in the initial condition (not shown).

3. The origin of the problem

To narrow down the necessary conditions for the existence of the spurious motions, we perform a one-hour simulation of the ARM SGP stratocumulus case, with $\Delta t=0.5$ s and $N_{aco}=6$, using a “stripped-down” 2-D version of WRF in which the microphysics, radiation, and SGS turbulence parameterizations are all turned off. The Coriolis parameter is also set to zero and the surface heat, moisture, and momentum fluxes are turned off. The model resolution is kept the same as in the 3-D simulations discussed above. The model domain is set to 5 km in the vertical direction and 4 km in the horizontal direction (i.e., 40 grid points across). The initial wind in the horizontal direction is set to 12 m s^{-1} and uniform in the vertical. Figure 10a shows the X-Z cross-section of perturbation vertical velocity, w' , 40 minutes after initialization. The spurious motions near the inversion are quite similar to those in the 3-D full-physics simulations in Section 2.2. This confirms that the spurious motions originate from the dynamical core, rather than from any physical parameterizations. We hereafter refer to this simulation as the “2-D test”.

The analysis suggests that (1) the spurious motions near the inversion and the sensitivity to time-stepping, especially acoustic sub-stepping, originate from the dynamical core in WRF, and (2) the spurious motions are very sensitive to the moisture jump and horizontal wind speed at the inversion layer. The following explanation of the WRF dynamical core’s treatment of moisture on the acoustic sub-steps elucidates how these issues can arise.

Historically, the time-split numerics in WRF for integrating the dynamical equations have solved prognostic equations for the flux-form variables $\vec{V} = \mu_d \vec{v} = (\mathbf{U}, \mathbf{V}, \Omega)$, $\theta = \mu_d \theta$, and μ_d on the acoustic sub-steps since these equations contain the terms that are fundamentally responsible for the propagation of acoustic and gravity waves [see Klemp et al. 2007; Skamarock et al. 2008 and references therein]. Here, \vec{v} represents the covariant

components of the velocity, θ is the potential temperature, and μ_d is the dry air mass per unit area in the column (i.e., the dry hydrostatic pressure difference between the surface and the model top). Moisture variables (including q_v) and other scalars are advanced on the larger dynamic time steps (i.e., the Runge-Kutta time steps). The pressure, p , must also be solved on the acoustic sub-steps, and is obtained from the ideal gas law:

$$p = p_0 \left(\frac{R_d \theta \left(1 + \frac{R_v}{R_d} q_v^t \right)}{p_0 \alpha_d \mu_d} \right)^\gamma \quad (1)$$

where p_0 is a reference pressure, R_d and R_v are the gas constants of dry air and water vapor, respectively, and $\gamma = c_p/c_v$ is the ratio of heat capacities for dry air. $\alpha_d = 1/\rho_d$, is the inverse of dry air density. Recognizing that the moisture variables are stepped forward on the dynamic time steps and therefore are not varying during the acoustic sub-steps, q_v is held fixed at q_v^t during the acoustic sub-steps, where the t superscript indicates values at the current Runge-Kutta time step.

This approach in time-splitting the numerical integration has proven to be robust over a wide spectrum of applications. However, in simulations with a large vertical gradient in moisture (near discontinuity) at high resolution, ignoring variations in q_v during the acoustic sub-steps may no longer serve as an accurate approximation.

4. The solution

To resolve this deficiency, we define a moist potential temperature $\theta_m = \mu_d \theta_m = \mu_d \theta \left(1 + \frac{R_v}{R_d} \right) q_v$ as the prognostic variable instead of θ . With this modification, the prognostic equation for θ is replaced by:

$$\partial_t \theta_m + (\nabla \cdot \vec{V} \theta_m)_\eta = F_{\theta_m}, \quad (2)$$

which has exactly the same form as the θ equation (see Klemp et al. 2007, Equation (24)), with θ_m replacing θ and F_θ suitably modified to F_{θ_m} . The gas law is then expressed as

$$p = p_0 \left(\frac{R_d \theta_m}{p_0 \alpha_d \mu_d} \right)^\gamma, \quad (3)$$

in which q_v no longer appears explicitly. Thus, by folding q_v into the θ_m variable, variations in q_v are implicitly accommodated during the acoustic sub-steps without the need to update q_v explicitly on these steps. The pressure can then be advanced on these sub-steps using Equation (3), in which all variables on the right-hand side are also updated on these same sub-steps. This procedure for representing moisture on the acoustic sub-steps using a prognostic θ_m variable is the same as that implemented by Skamarock et al. [2012] for the time-split numerical scheme used by the global Model for Prediction Across Scales (MPAS).

The effectiveness of the proposed modification is demonstrated in the next two sections for the DYCOMS-II RF02 and ARM SGP stratocumulus cases.

4.1 DYCOMS-II RF02 case

The dynamical core modifications in WRF eliminate the spurious fluctuations for the DYCOMS-II RF02 case (not shown) and the convergence problem is also resolved for this case, as shown in Figure 11. While the original model produces different values of LWP, cloud-top and base heights, and total cloud fraction for $N_{aco}=6$ and $N_{aco}=12$, the simulations using the modified model show a clear convergence.

4.2 ARM SGP stratocumulus case

Repeating the 2-D test from Section 3 with the modified dynamical core shows clearly that the spurious motions near the inversion are absent (Figure 10b). We also repeat the four 3-D full physics simulations described in Section 2.2 using WRF v3.6.1 with the modified dynamical core. Figure 12 shows the evolution of total cloud fraction and LWP for the four simulations in the same format as Figure 8. Comparing the two figures, one can clearly see that the convergence issue is resolved with the modified model. The simulated total cloud fraction and LWP all converge to virtually the same values. Note also that the original model using $\Delta t=0.5$ s and $N_{aco}=12$ (the black solid lines in Figure 8) produces total cloud fraction and LWP very close to those produced by the modified model. This implies that for this particular case and setup, $\Delta t=0.5$ s and $N_{aco}=12$ are close to the lowest temporal resolution needed for convergence without the modifications and, with the modifications one can expect the simulations to converge at $\Delta t=1.0$ s and $N_{aco}=6$ or even

less conservative time settings. The spurious motions near the inversion (Figure 9) are also completely eliminated in the simulations with the modified model (not shown).

5. Conclusions and discussion

In this study, we investigate the sensitivity of cloud properties to time-stepping choices in WRF large-eddy simulations of stratocumulus clouds, which has previously been noted by Yamaguchi and Feingold [2012]. We examine the sensitivity in two stratocumulus cases: one marine, the GCSS DYCOMS-II RF02 case, and one continental, a stratocumulus case over the ARM SGP site on 13 May 2008.

We demonstrate that, in both cases, the sensitivity is associated with spurious motions near the inversion at the boundary layer top. Decreasing the temporal resolution, by increasing Δt or decreasing N_{aco} , increases the magnitude of the spurious signal, giving rise to the sensitivity seen in the cloud fraction and LWP. The spurious signal is very sensitive to (1) the moisture jump across the inversion (the stronger the moisture jump, the stronger the signal) and (2) the mean horizontal wind in the inversion layer (the spurious motions vanish if we set the mean wind to zero). Furthermore, the spurious motions persist in a 2-D setup of WRF with all physical parameterizations and external forcings turned off (including mean wind shear and Coriolis effect) for the ARM SGP stratocumulus case. All these clues point to the WRF dynamical core being the issue, rather than the physics parameterizations, and examination of assumptions within the dynamical core suggests the problem lies in the treatment of moisture on the acoustic sub-steps.

In WRF, water vapor mixing ratio (q_v) is integrated only on the larger dynamic time steps. In the calculation of pressure on the acoustic sub-steps, the effect of moisture perturbations from sub-step to sub-step is assumed to be negligible. This assumption becomes problematic in simulations with very large vertical moisture gradients, where moisture perturbations during the acoustic sub-steps can become large.

We suggest modifying the WRF dynamical core such that θ_m is the prognostic variable instead of θ . This equates to using Equation (3) (instead of (1)) in the calculation of pressure on the acoustic sub-steps. Our results show that this modification prevents the spurious motions from forming and removes the sensitivity to time-stepping choices in

both the marine and continental stratocumulus cases. WRF version 3.7, now available to the community, has incorporated our modification as an option for LES.

Implied in the results presented here is that the modification to the dynamical core permits the use of longer time steps and fewer acoustic sub-steps than in the original version of WRF. This has the advantage of making the model simulations computationally cheaper. The purpose of this paper is not to test the limits of the time step settings; however, we note that time steps twice as long as previously used now give similar results as shorter time steps.

In retrospect, the convergence issue arises through the choice of prognostic variables used in the dynamic equations under the time-split integration framework. The two stratocumulus cases discussed here highlight the scenario where water vapor plays an active role in the “dry” dynamics, hence the need to carry the moist potential temperature θ_m as a prognostic variable on the acoustic time step.

The problems that we have illustrated for LES applications within the original WRF model formulation (using θ as opposed to θ_m as a prognostic variable) have not been observed in other LES models (e.g. the LES models described in Stevens et al. 2005 and references therein). Most existing moist LES models use as a prognostic variable some form of potential temperature coupled with moisture, for example the virtual potential temperature or some form of moist static energy, and as such, moisture is taken into account in the dynamic time step. In addition, not all LES models are compressible, and of those that admit acoustic waves only a few use a time-split integration technique that would be susceptible to the problems we have discussed. Recently developed nonhydrostatic compressible atmospheric solvers using height coordinates and cast in conservative form are using θ_m or θ_v as illustrated by MPAS [Skamarock et al. 2012] and the ICOSahedral Nonhydrostatic (ICON) model [Zängl et al. 2014], respectively. Models using non-conservative formulations, such as the Coupled Ocean-Atmosphere Mesoscale Prediction System (COAMPS, Hodur 1997), the Advanced Regional Prediction System (ARPS, Xue et al. 2000), and the Regional Atmospheric Modeling System (RAMS, Pielke et al. 1992) have not incorporated moisture into the thermodynamic equation on the acoustic

steps in their time-split integrations. A number of new nonhydrostatic compressible model formulations are being developed because of the capabilities of new computers to accommodate global cloud-permitting simulations, some of which are time-split. We do not know if the problems exhibited in the LES regime exist in some form at coarser grid spacings, and existing and new nonhydrostatic solver formulations should be examined for susceptibility to these problems. In the future, the development of compressible dynamical cores using similar time-split methods should take into account our finding in the design of the equation system, especially when choosing prognostic variables for the system.

Acknowledgements

The authors thank Branko Kosovic for his suggestions with this research. This research is based on work supported by the U.S. Department of Energy Office of Biological and Environmental Research as part of the Atmospheric System Research Program and a DOE Early Career award to Gustafson. The research conducted at Brookhaven National Laboratory was supported by the Atmospheric System Research Program via DE-SC00112704. Data was used from the Atmospheric Radiation Measurement Climate Research Facility, a DOE Office of Science User Facility. We gratefully acknowledge the usage of the WRF LES package from Dr. Tak Yamaguchi (available at <http://esrl.noaa.gov/csd/staff/tak.yamaguchi/code/>). The Pacific Northwest National Laboratory is operated for DOE by Battelle Memorial Institute under contract DE-AC05-76RL01830. A portion of this research was performed using the Environmental Molecular Sciences Laboratory, a DOE Office of Science user facility sponsored by the Department of Energy's Office of Biological and Environmental Research and located at Pacific Northwest National Laboratory, and PNNL Institutional Computing at Pacific Northwest National Laboratory. The newest WRF version can be downloaded from <http://wrf-model.org>. The simulation data used in this paper will be made available upon request to the first author.

References

- Ackerman, A. S., and Coauthors (2009), Large-eddy simulations of a drizzling, stratocumulus-topped marine boundary layer, *Mon. Wea. Rev.*, 137, 1083–1110.
- Atmospheric Radiation Measurement (ARM) Climate Research Facility, (1994), updated yearly. ARM Best Estimate Data Products (ARMBEATM). 05-13-2008, 36.605 N 97.485 W: Southern Great Plains (SGP) Central Facility, Lamont, OK (C1). Compiled by R. McCoy and S. Xie. Atmospheric Radiation Measurement (ARM) Climate Research Facility Data Archive: Oak Ridge, Tennessee, USA. Data set accessed 10-01-2014 at <http://dx.doi.org/10.5439/1039931>.
- Atmospheric Radiation Measurement (ARM) Climate Research Facility (1996), updated hourly. MWR Retrievals (MWRRET1LILJCLOU). 05-13-2008, 36.605 N 97.485 W: Southern Great Plains (SGP) Central Facility, Lamont, OK (C1). Compiled by K. Gaustad and L. Riihimaki. Atmospheric Radiation Measurement (ARM) Climate Research Facility Data Archive: Oak Ridge, Tennessee, USA. Data set accessed 10-01-2014 at <http://dx.doi.org/10.5439/1027369>.
- Atmospheric Radiation Measurement (ARM) Climate Research Facility (2000), updated hourly. Total Sky Imager (TSISKYCOVER). 05-13-2008, 36.605 N 97.485 W: Southern Great Plains (SGP) Central Facility, Lamont, OK (C1). Compiled by V. Morris. Atmospheric Radiation Measurement (ARM) Climate Research Facility Data Archive: Oak Ridge, Tennessee, USA. Data set accessed 10/01/2014 at <http://dx.doi.org/10.5439/1025308>.
- Blossey, P. N., C. S. Bretherton, M. Zhang, A. Cheng, S. Endo, T. Heus, Y. Liu, A. P. Lock, S. R. de Roode, and K.-M. Xu (2013), Marine low cloud sensitivity to an idealized climate change: The CGILS LES intercomparison, *J. Adv. Model. Earth Syst.*, 5, 234–258, doi:10.1002/jame.20025.
- Deardorff, J. W. (1980), Stratocumulus-capped mixed layers derived from a three-dimensional model, *Bound.-Layer Meteor.*, 18, 495–527.
- Endo, S, A. M. Fridlind, W. Lin, A. M. Vogelmann, T. Toto, A. S. Ackerman, G. M. McFarquhar, R. C. Jackson, H. H. Jonsson, and Y. Liu (2015), RACORO continental boundary layer cloud investigations. Part II: Large-eddy simulations of cumulus clouds and evaluation with in-situ and ground-based observations, *J. Geophys. Res. Atmos.*, 120, doi: 10.1002/2014JD022525.
- Hodur, R. (1997). The Naval Research Laboratory's coupled ocean/atmosphere mesoscale prediction system (COAMPS). *Mon. Wea. Rev.*, 125(7), 1414-1430.
- Iacono, M., J. Delamere, E. Mlawer, M. Shephard, S. Clough, and W. Collins (2008), Radiative forcing by long-lived greenhouse gases: Calculations with the AER radiative transfer models, *J. Geophys. Res.*, 113, D13103, doi:10.1029/2008JD009944.

Klemp, J. B., and R. Wilhelmson (1978), The simulation of three-dimensional convective storm dynamics, *J. Atmos. Sci.*, 35, 1070–1096.

Klemp, J. B., W. C. Skamarock, and J. Dudhia, (2007), Conservative split-explicit time integration methods for the compressible nonhydrostatic equations, *Mon. Wea. Rev.*, 135, 2897–2913.

Lin, Yuh-Lang, Richard D. Farley, and Harold D. Orville (1983), Bulk Parameterization of the Snow Field in a Cloud Model, *J. Climate Appl. Met.*, 22, 1065–1092.

Liu, X, S. Osher, and T. Chen (1994), Weighted Essentially Non-Oscillatory Schemes, *J. Comp. Phys.*, 115, 200–212. DOI:10.1006/jcph.1994.1187.

Moeng, C.-H., J. Dudhia, J. Klemp, and P. Sullivan (2007), Examining Two-Way Grid Nesting for Large Eddy Simulation of the PBL Using the WRF Model, *Mon. Wea. Rev.*, 135, 2295–2311.

Morrison, H., G. Thompson, V. Tatarskii (2009), Impact of Cloud Microphysics on the Development of Trailing Stratiform Precipitation in a Simulated Squall Line: Comparison of One- and Two-Moment Schemes. *Mon. Wea. Rev.*, 137, 991–1007.

Pielke R. A. , W. R. Cotton, R. L. Walko, C. J. Trembaek, W. A. Lyons, L. D. Grasso, M. E. Nieholls, M. D. Moran, D. A. Wesley, T. J. Lee, and J. H. Copeland (1992). A Comprehensive Meteorological Modeling System- RAMS, *Meteorology And Atmospheric Physics*, 49, 69-91.

Skamarock, W. C, J. B. Klemp, M. G. Duda, L. Fowler, S.-H. Park, and T. D. Ringler, 2012: A Multi-scale Nonhydrostatic Atmospheric Model Using Centroidal Voronoi Tessellations and C-Grid Staggering. *Mon. Wea. Rev.*, 240, 3090-3105

Skamarock, W. C., J. B. Klemp, J. Dudhia, D. O. Gill, D. M. Barker, M. G. Duda, W. Wang, and J. G. Powers (2008), A description of the advanced research WRF version 3, 113 pp., NCAR Technical Note, NCAR/TN-475+STR, National Center for Atmospheric Research, Boulder, CO.

Stevens, B. and Coauthors (2003), Dynamics and Chemistry of Marine Stratocumulus—DYCOMS-II, *Bull. Amer. Meteorol. Soc.*, 84, 579-593.

Stevens, B., and Coauthors (2005), Evaluation of large-eddy simulations via observations of nocturnal marine stratocumulus, *Mon. Wea. Rev.*, 133, 1443–1462.

Turner, D. D., S. A. Clough, J. C. Liljegren, E. E. Clothiaux, K. Cady-Pereira, and K. L. Gaustad (2007), Retrieving liquid water path and precipitable water vapor from Atmospheric Radiation Measurement (ARM) microwave radiometers. *IEEE Trans. Geosci. Remote Sens.*, 45, 3680–3690, doi:10.1109/TGRS.2007.903703.

Wang, H., and G. Feingold (2009a), Modeling mesoscale cellular structures and drizzle in marine stratocumulus. Part I: Impact of drizzle on the formation and evolution of open cells, *J. Atmos. Sci.*, 66, 3237–3255.

Wang, H., and G. Feingold (2009b), Modeling mesoscale cellular structures and drizzle in marine stratocumulus. Part II: The Microphysics and Dynamics of the Boundary Region between Open and Closed Cells, *J. Atmos. Sci.*, 66, 3257–3275.

Wang, H., W. C. Skamarock, and G. Feingold (2009), Evaluation of scalar advection schemes in the Advanced Research WRF model using large-eddy simulations of aerosol-cloud interactions, *Mon. Wea. Rev.*, 137, 2547–2558.

Wicker, L. J. and W. C. Skamarock (2002), Time splitting methods for elastic models using forward time schemes, *Mon. Wea. Rev.*, 130, 2088–2097.

Xiao, Heng, W. I. Gustafson Jr. and H. Wang (2014), Impact of subgrid-scale radiative heating variability on the stratocumulus-to-trade cumulus transition in climate models, *J. Geophys. Res.-Atmospheres*, 119, 4192–4203, doi:10.1002/2013JD020999.

Xie, S., and Coauthors (2010), CLOUDS AND MORE: ARM Climate Modeling Best Estimate Data, *Bull. Amer. Meteor. Soc.*, 91, 13–20. DOI: 10.1175/2009BAMS2891.1.

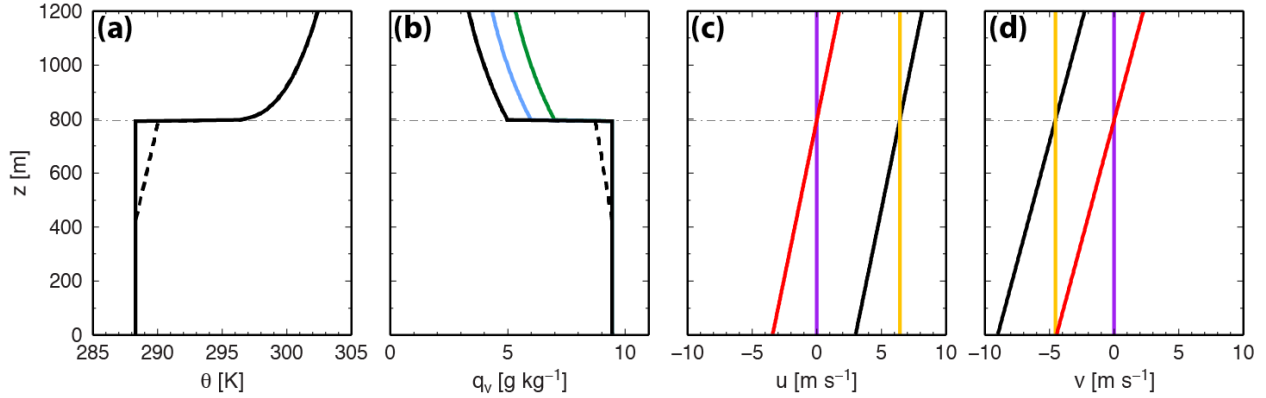
Xue, M., Droegemeier, K., & Wong, V. (2000). The Advanced Regional Prediction System (ARPS) - A multi-scale nonhydrostatic atmospheric simulation and prediction model. Part I: Model dynamics and verification. *Meteorology And Atmospheric Physics*, 75, 161–193.

Yamaguchi, T., and G. Feingold (2012), Technical note: Large-Eddy simulation of cloudy boundary layer with the Advanced Research WRF model, *J. Adv. Model. Earth Syst.*, 4, M09003, doi:10.1029/2012MS000164.

Yamaguchi T., W. Alan Brewer, and Graham Feingold (2013), Evaluation of Modeled Stratocumulus-Capped Boundary Layer Turbulence with Shipborne Data. *J. Atmos. Sci.*, 70, 3895–3919.

Zängl, G., Reinert, D., Rípodas, P., & Baldauf, M. (2014). The ICON (ICOsahedral Non-hydrostatic) modelling framework of DWD and MPI-M: Description of the non-hydrostatic dynamical core. Quarterly Journal Of The Royal Meteorological Society, ICON Non-Hydrostatic Dynamical Core, *Q. J. R. Meteorol. Soc.*, 141, 563–579. doi:10.1002/qj.2378

517 **Figures**



518
519 Figure 1: Initial profiles of (a) potential temperature (b) water vapor mixing ratio, and (c)
520 zonal and (d) meridional winds for the DYCOMS-II RF02 case control simulations (black
521 lines) and sensitivity simulations with a reduced moisture jump (1 g kg⁻¹ in blue line; 2 g
522 kg⁻¹ in green) and modified winds ('no wind' run with purple lines; 'no shear' run with
523 yellow lines; 'zero speed at inversion' run with red lines). The black dashed lines indicate
524 the values after condensation occurs in the first time step of the control simulation.

525

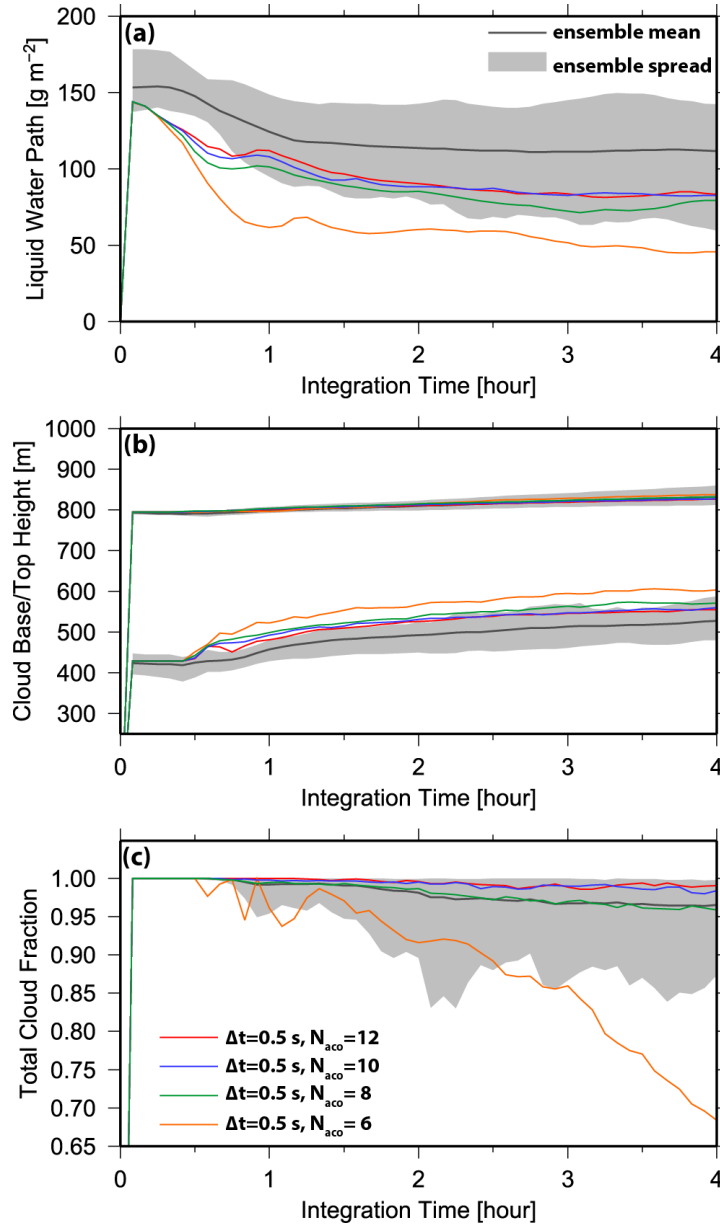


Figure 2: Time series of (a) LWP, (b) cloud-top and cloud-base heights, and (c) cloud fraction from the DYCOMS-II RF02 simulations using $\Delta t = 0.5$ s and $N_{\text{aco}} = 6, 8, 10$, and 12 (see colors in legend). Following Ackermann et al. [2009], cloud-top is defined as the height where domain-averaged total water = 8 g kg^{-1} and cloud fraction is defined as domain fraction of columns with column LWP $> 20 \text{ g m}^{-2}$. The ensemble mean (black line) and spread (gray shading) from simulations in the inter-comparison described in Ackerman et al. [2009] are shown for comparison.

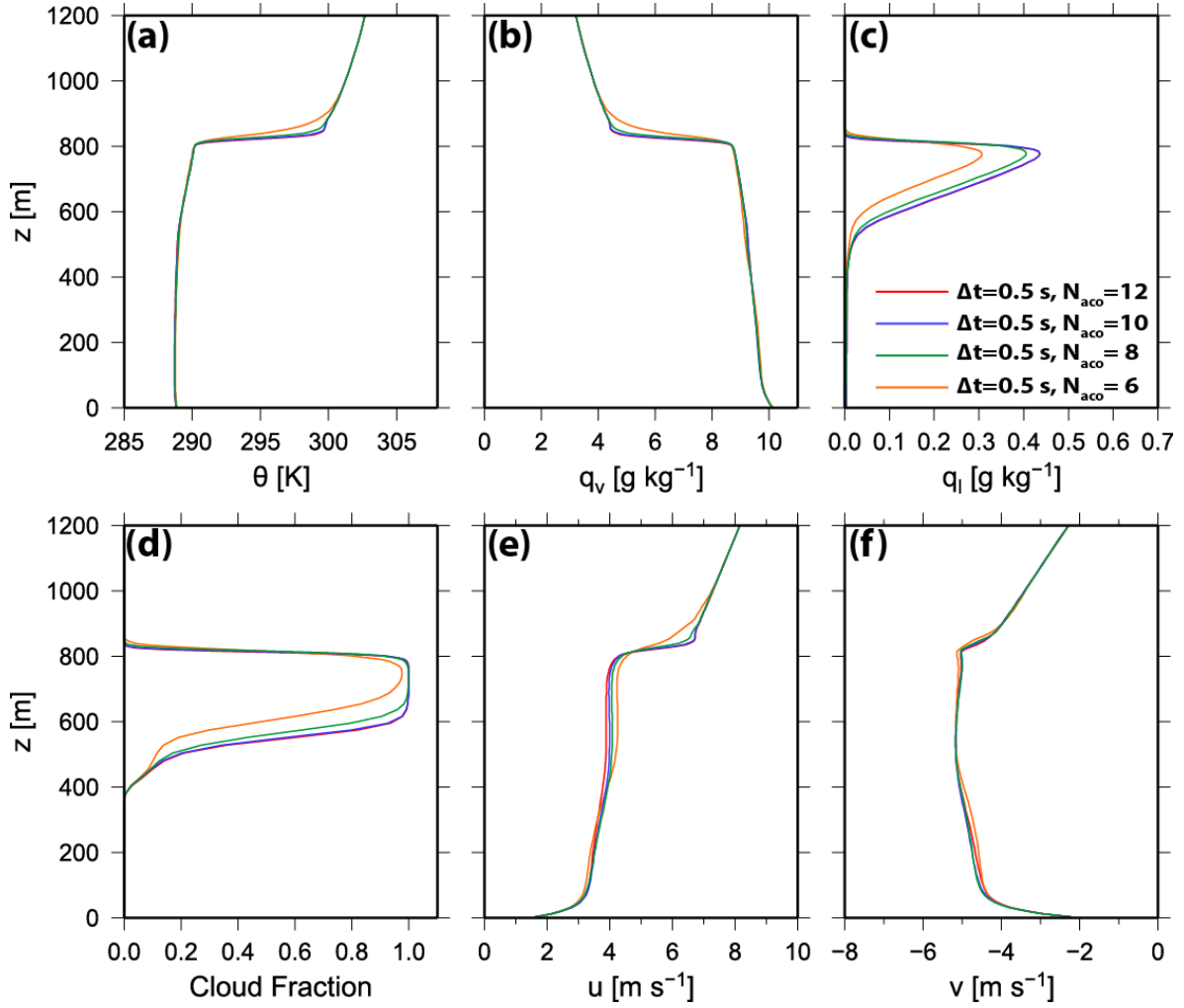


Figure 3: Vertical profiles of (a) potential temperature, (b) water vapor mixing ratio, (c) liquid water mixing ratio, (d) cloud fraction, and (e) zonal and (f) meridonal winds. Values are averages for hours 2 to 4 of the integration period for DYCOMS-II RF02 simulations using $N_{aco} = 6, 8, 10$, and 12.

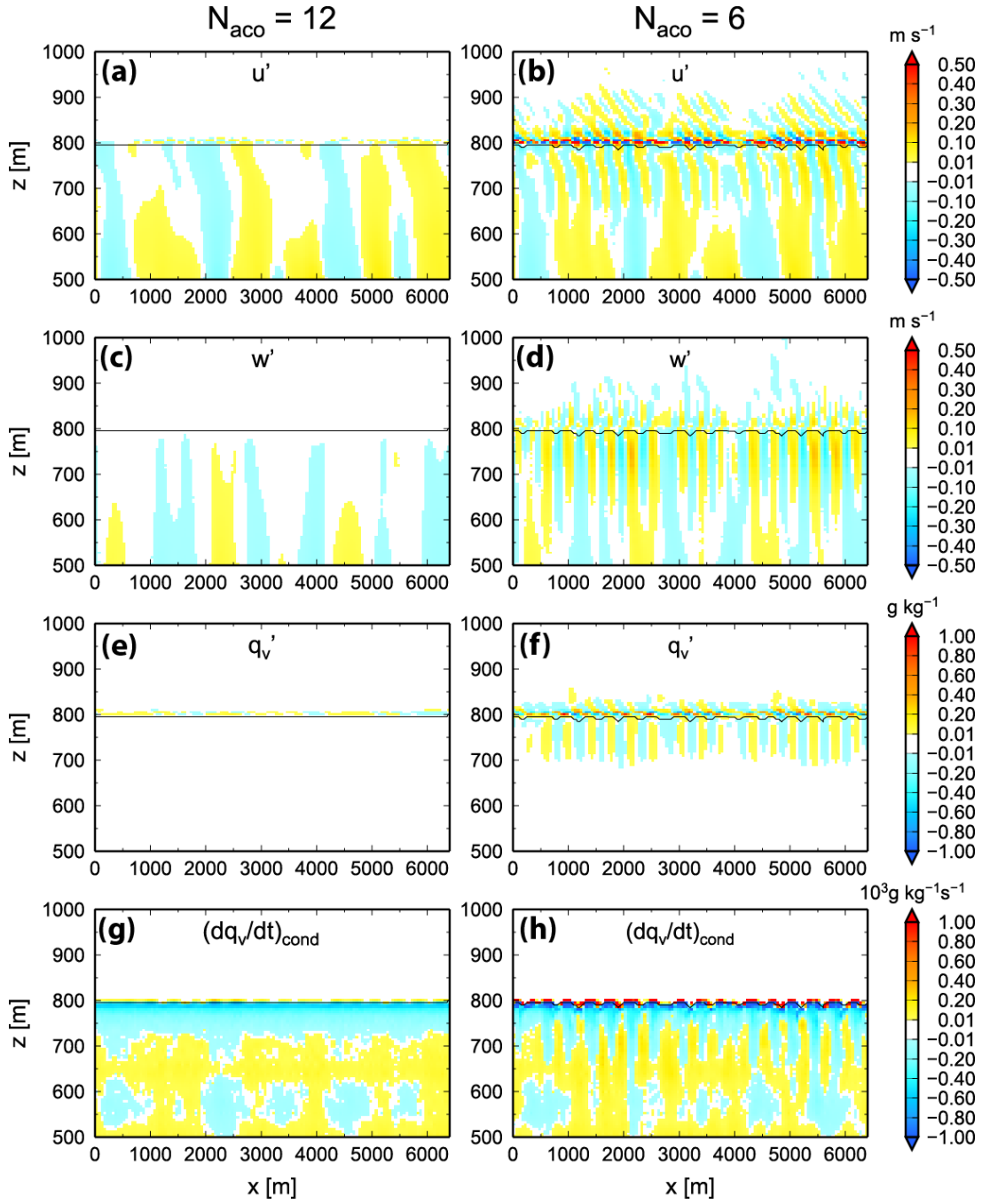


Figure 4: Vertical cross section of (a-b) zonal wind perturbation, u' (m s^{-1}), (c-d) vertical wind perturbation, w' (m s^{-1}), (e-f) water vapor mixing ratio perturbation, q_v' (g kg^{-1}), and (g-h) water vapor tendency due to evaporation and condensation, $(dq_v/dt)_{\text{cond}}$ ($\text{g kg}^{-1} \text{s}^{-1}$), 30 minutes into the DYCOMS-II RF02 simulation period using $N_{\text{aco}} = 6$ (right) and 12 (left).

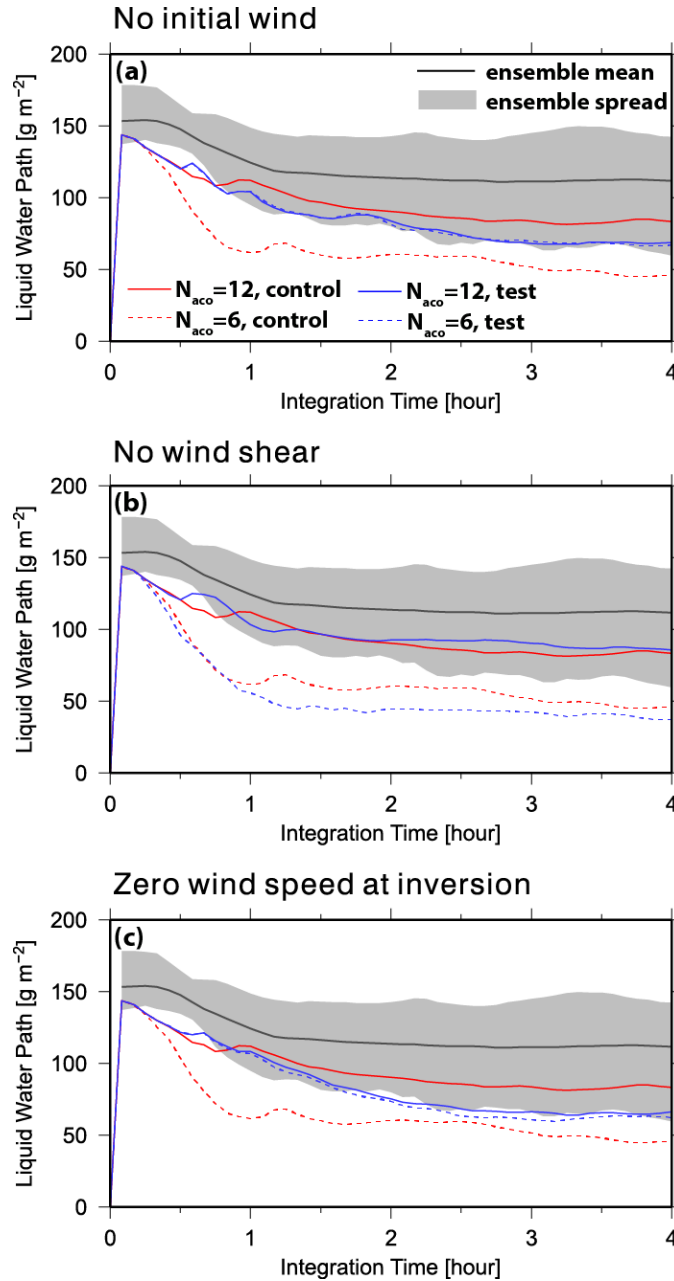


Figure 5: Time series of LWP (g m^{-2}) from the initial wind sensitivity tests of the DYCOMS-II RF02 case, as described in the text. Large differences between the solid and dashed blue lines indicate the presence of the convergence issue. Note the sensitivity simulations converge to a different solution than the control simulation (solid red line) because of changes in initial wind profiles.

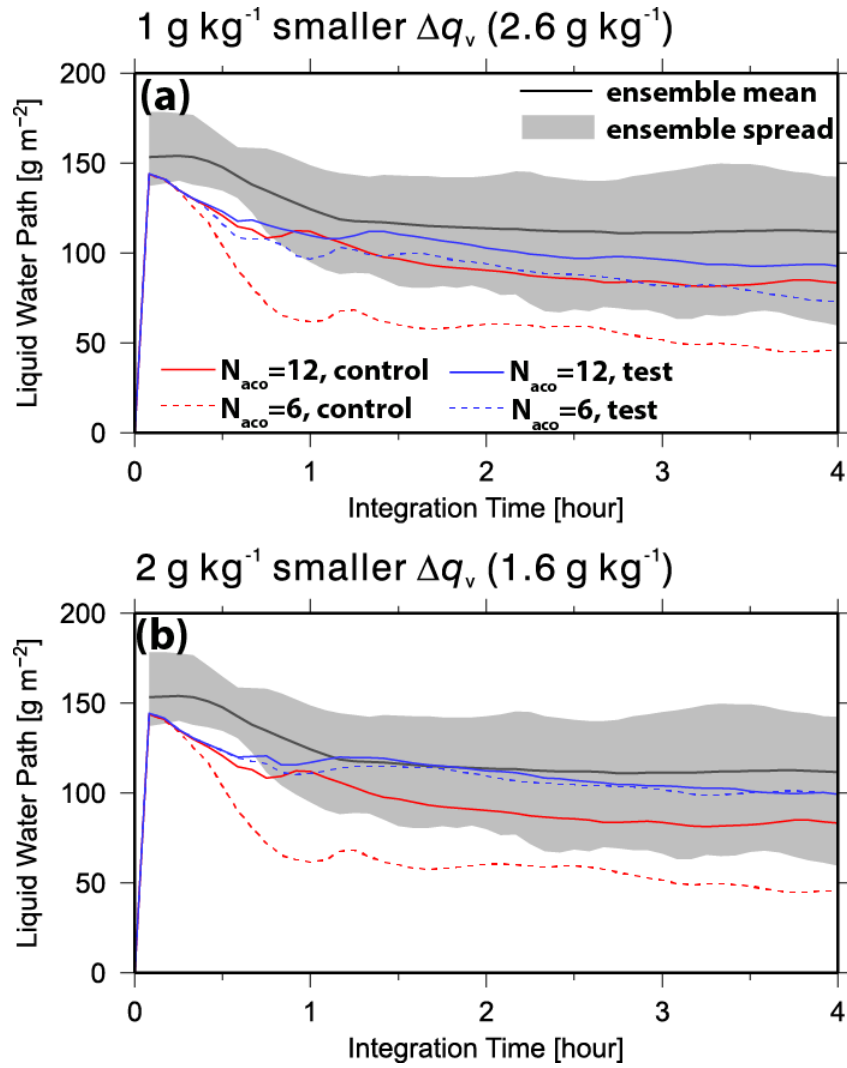


Figure 6: As in Figure 5, except for sensitivity tests with reduced moisture jumps across the inversion.

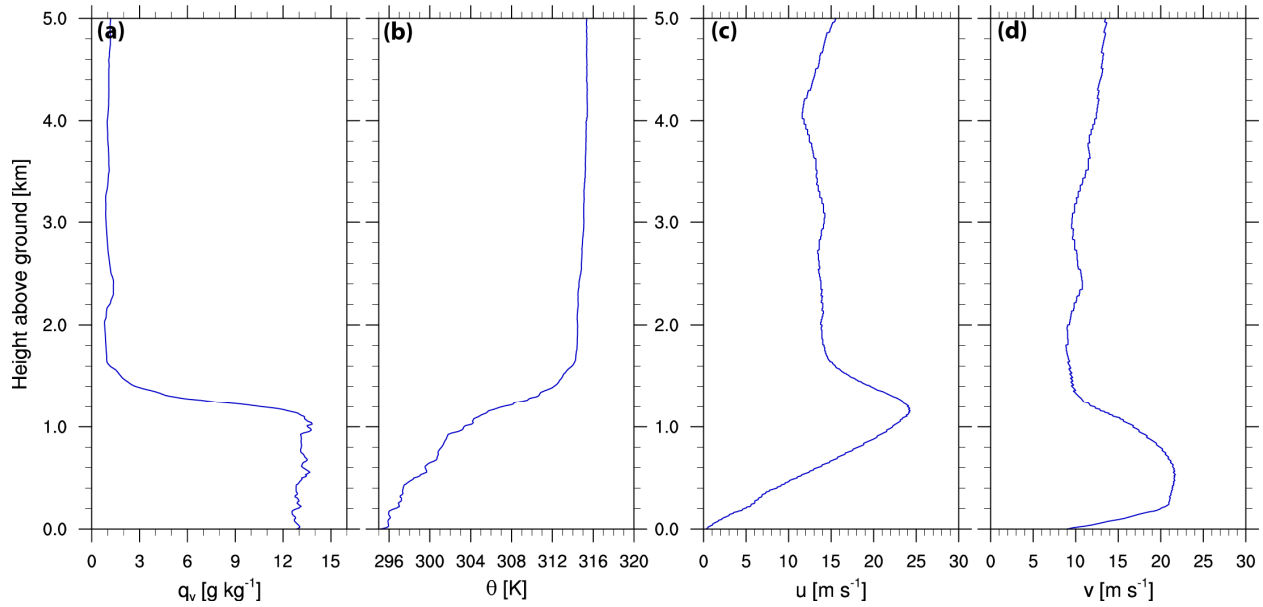


Figure 7: The profiles of (a) water vapor mixing ratio (g kg^{-1}), (b) potential temperature (K), (c) zonal and (d) meridional winds (m s^{-1}) from the 1130 UTC sounding at the ARM SGP site on May 13 2008.

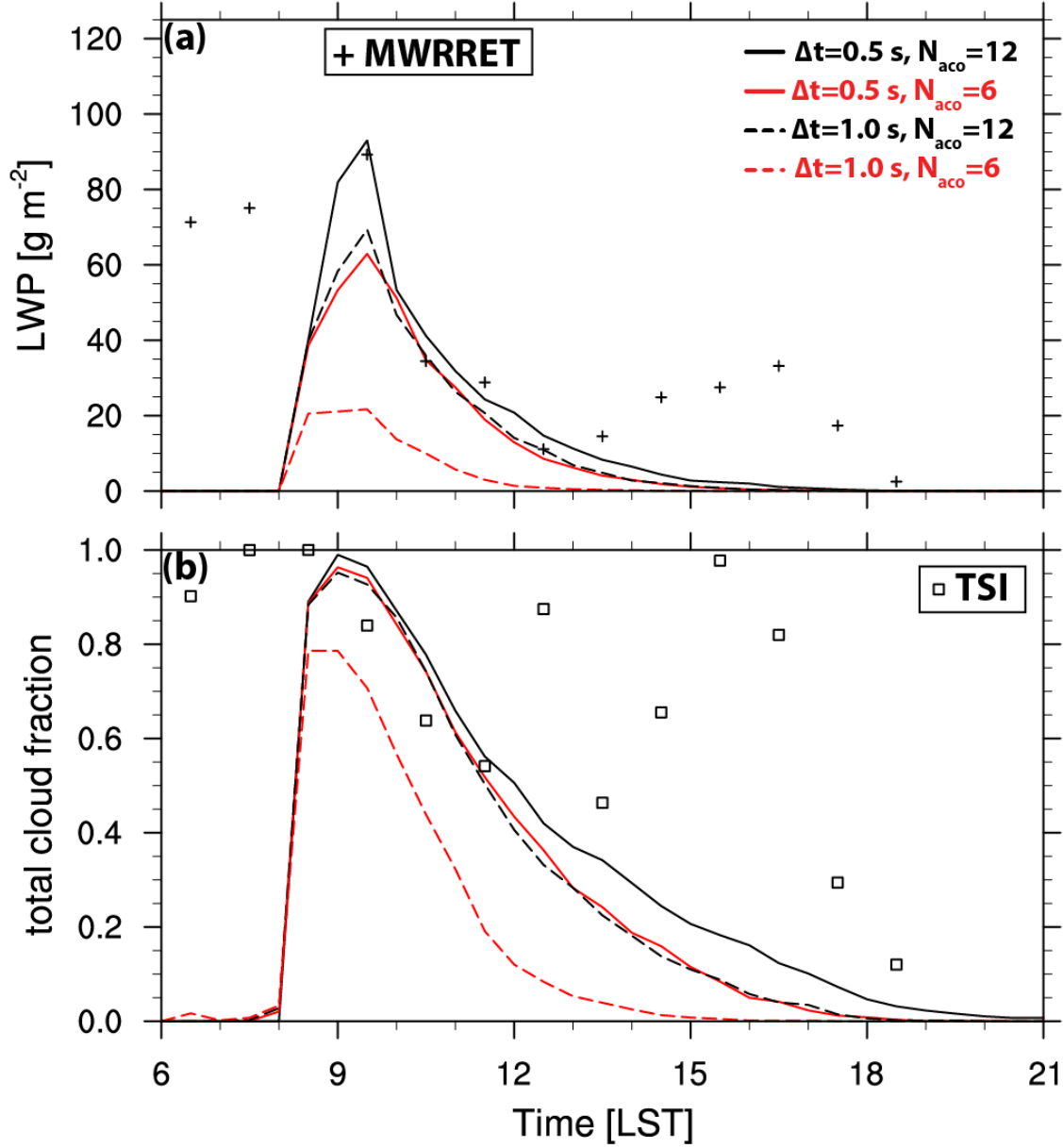


Figure 8: (a) The LWP (g m^{-2}) and (b) total cloud fraction of the four WRF simulations of the SGP stratocumulus case with different time stepping choices. MWRRET LWP and TSI cloud fraction observations from the ARM SGP site are shown for comparison.

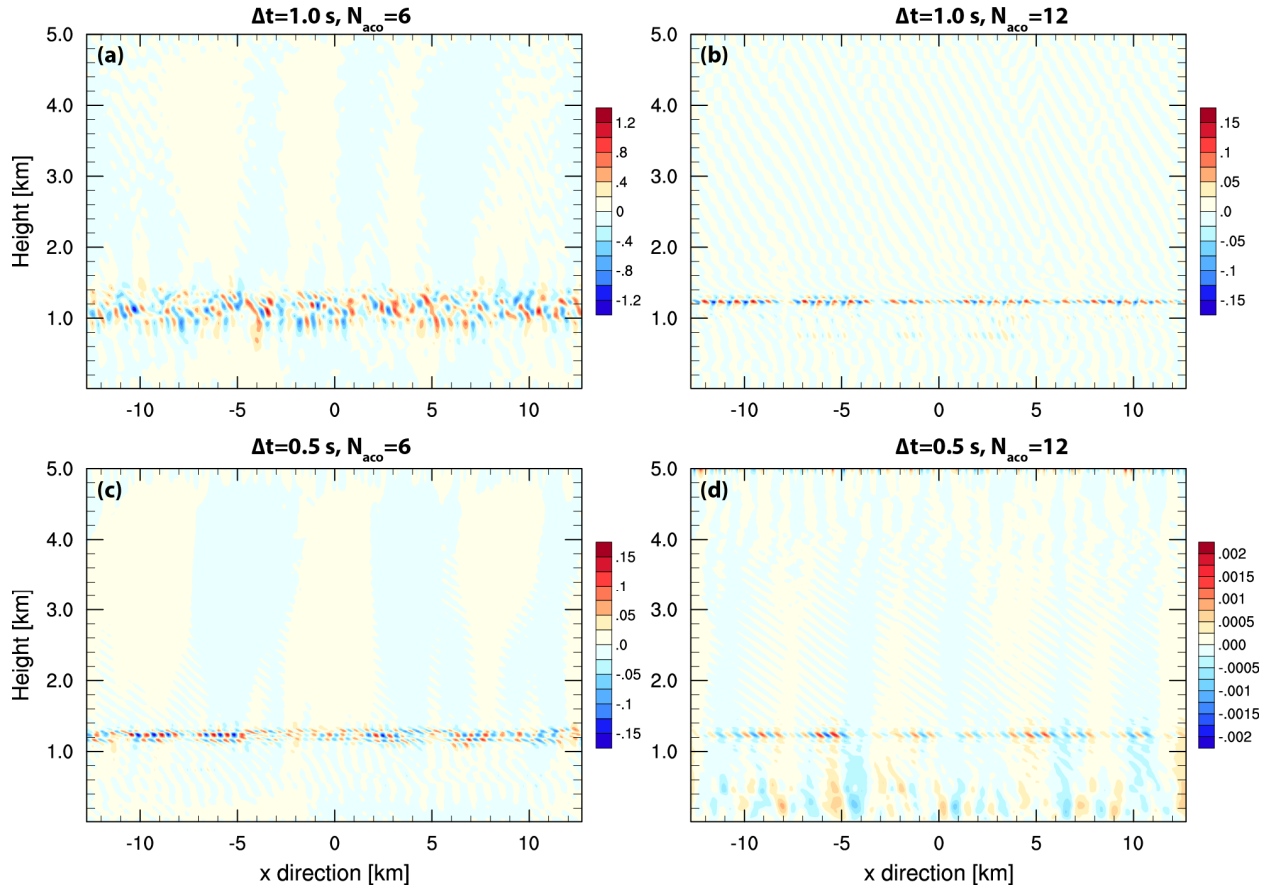


Figure 9: The X-Z cross-section of w' (deviation from horizontal mean, m s^{-1}) at $t=30$ minutes for the WRF simulations of the SGP stratocumulus case using (a) $\Delta t=1.0 \text{ s}$, $N_{\text{aco}}=6$, (b) $\Delta t=1.0 \text{ s}$, $N_{\text{aco}}=12$, (c) $\Delta t=0.5 \text{ s}$, $N_{\text{aco}}=6$ and (d) $\Delta t=0.5 \text{ s}$, $N_{\text{aco}}=12$. Note that different panels use different color scales.

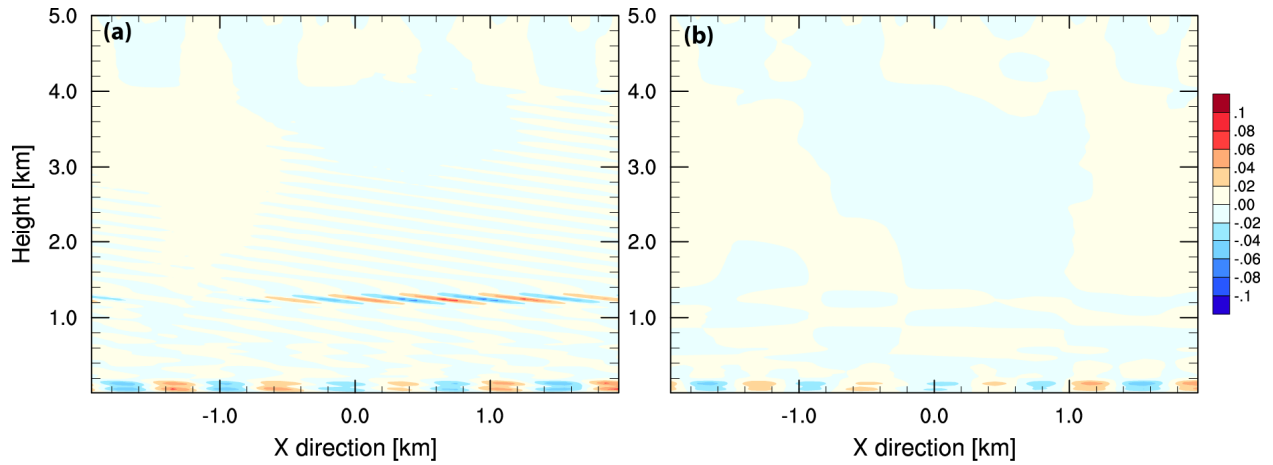


Figure 10: The X-Z cross-section of w' (deviation from horizontal mean, m s^{-1}) at $t=40$ minutes for the WRF 2-D test simulation of the SGP stratocumulus case with (a) the original WRF and (b) the modified dynamical core in WRF.

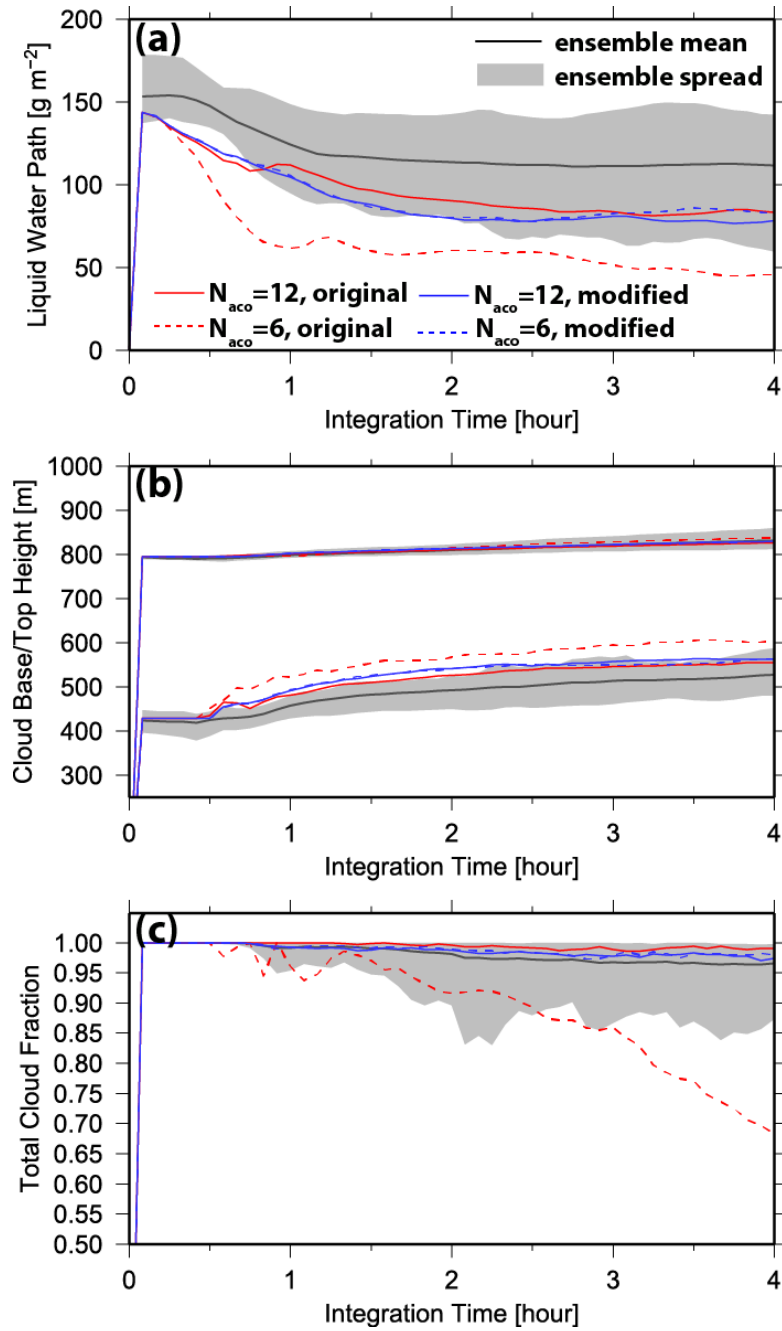
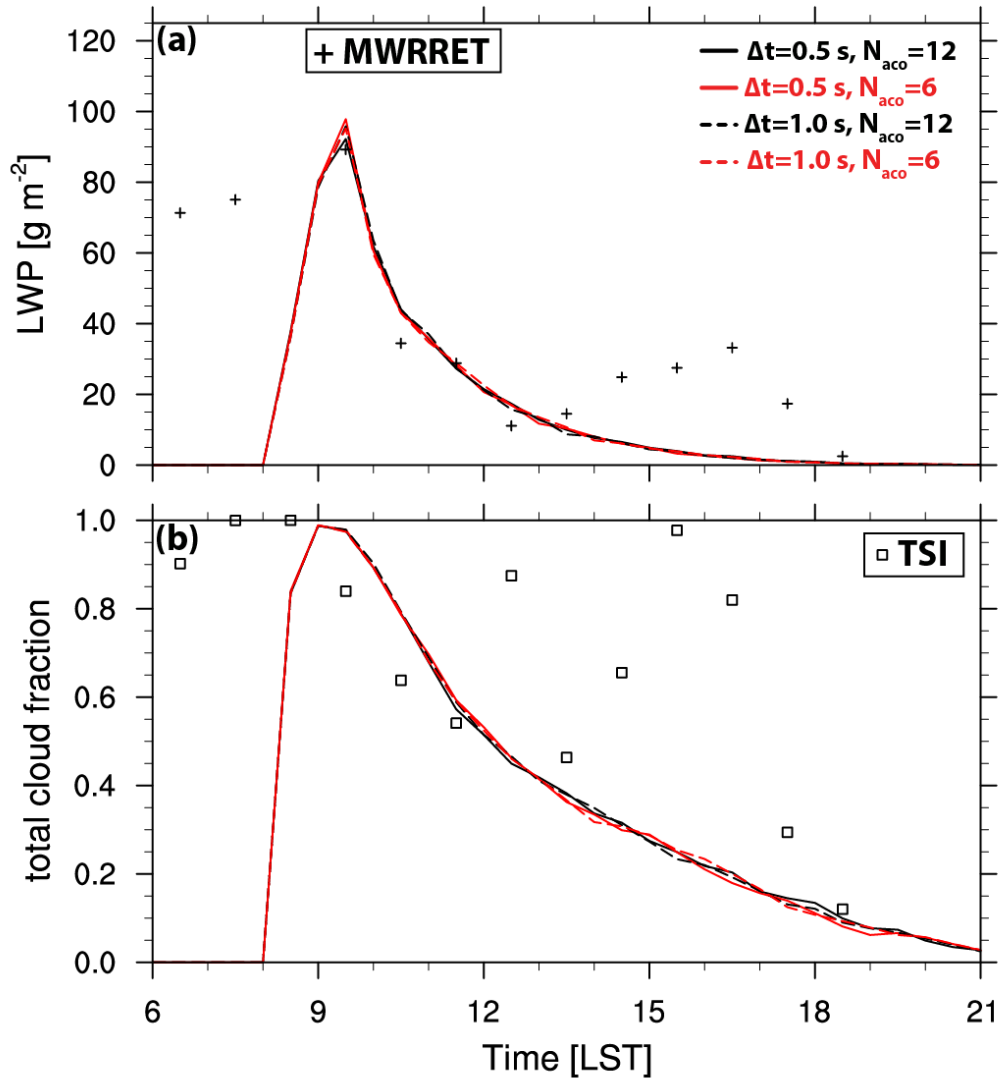
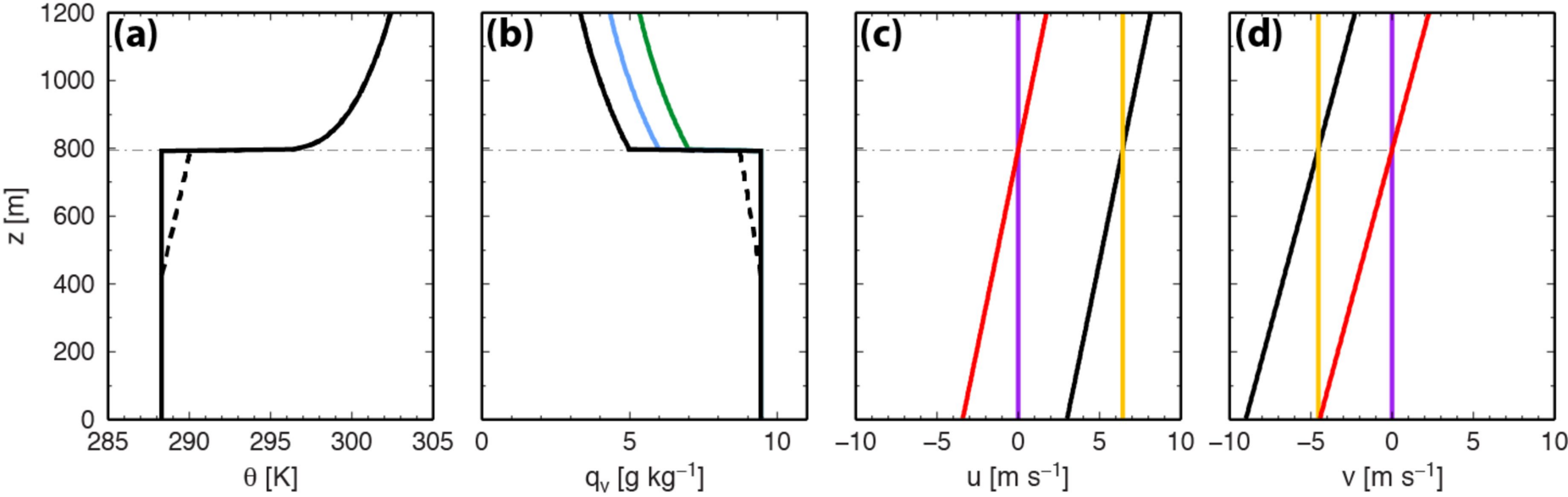


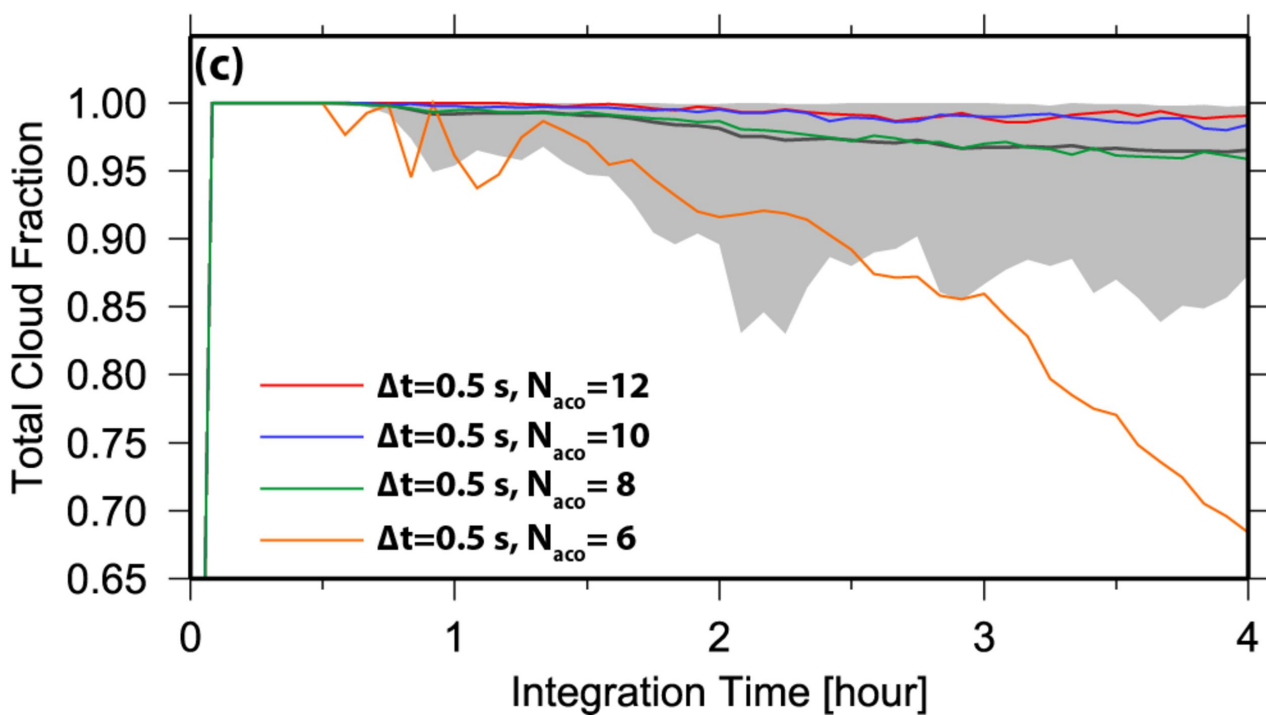
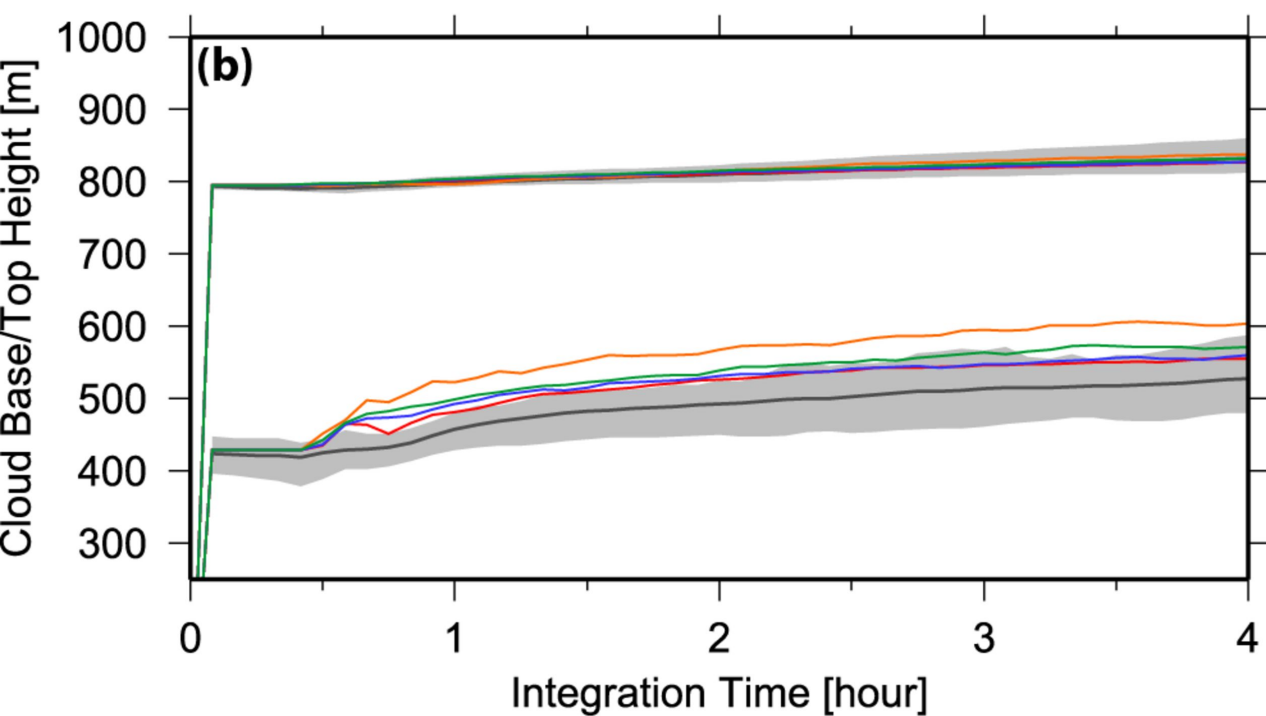
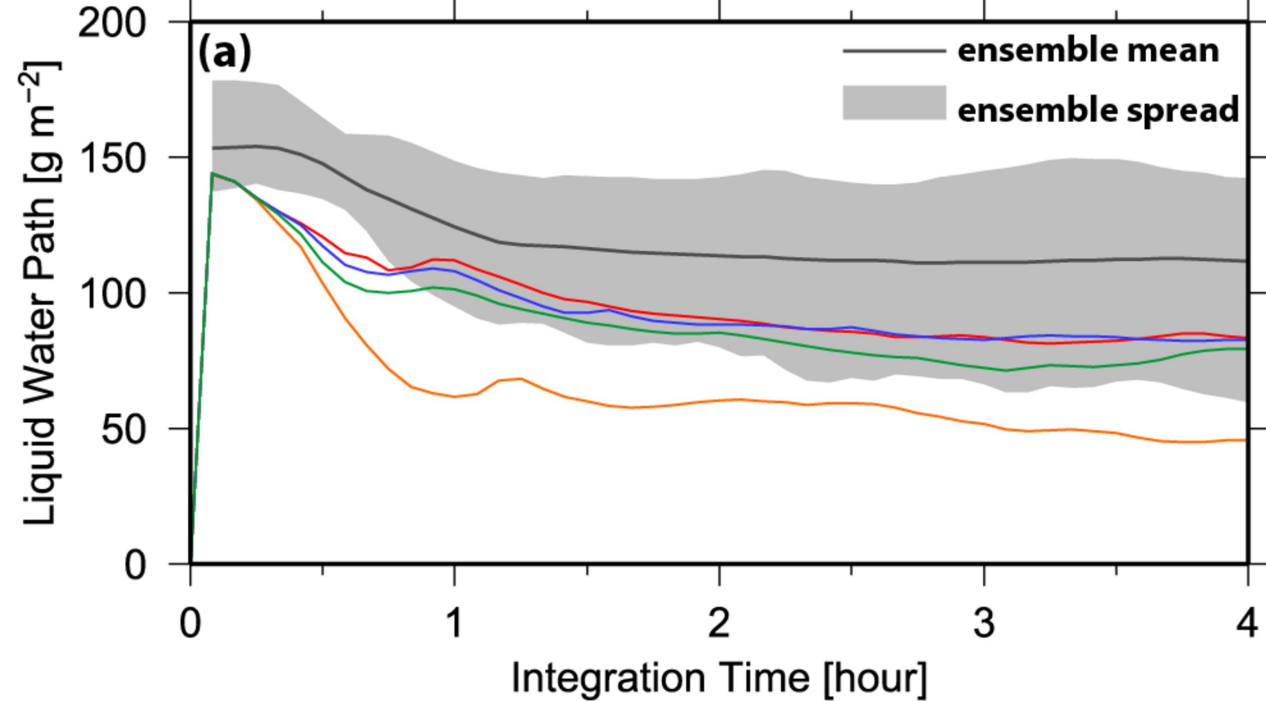
Figure 11: As in Figure 2, except for the simulations using the modified dynamical core for the DYCOMS-II RF02 case.

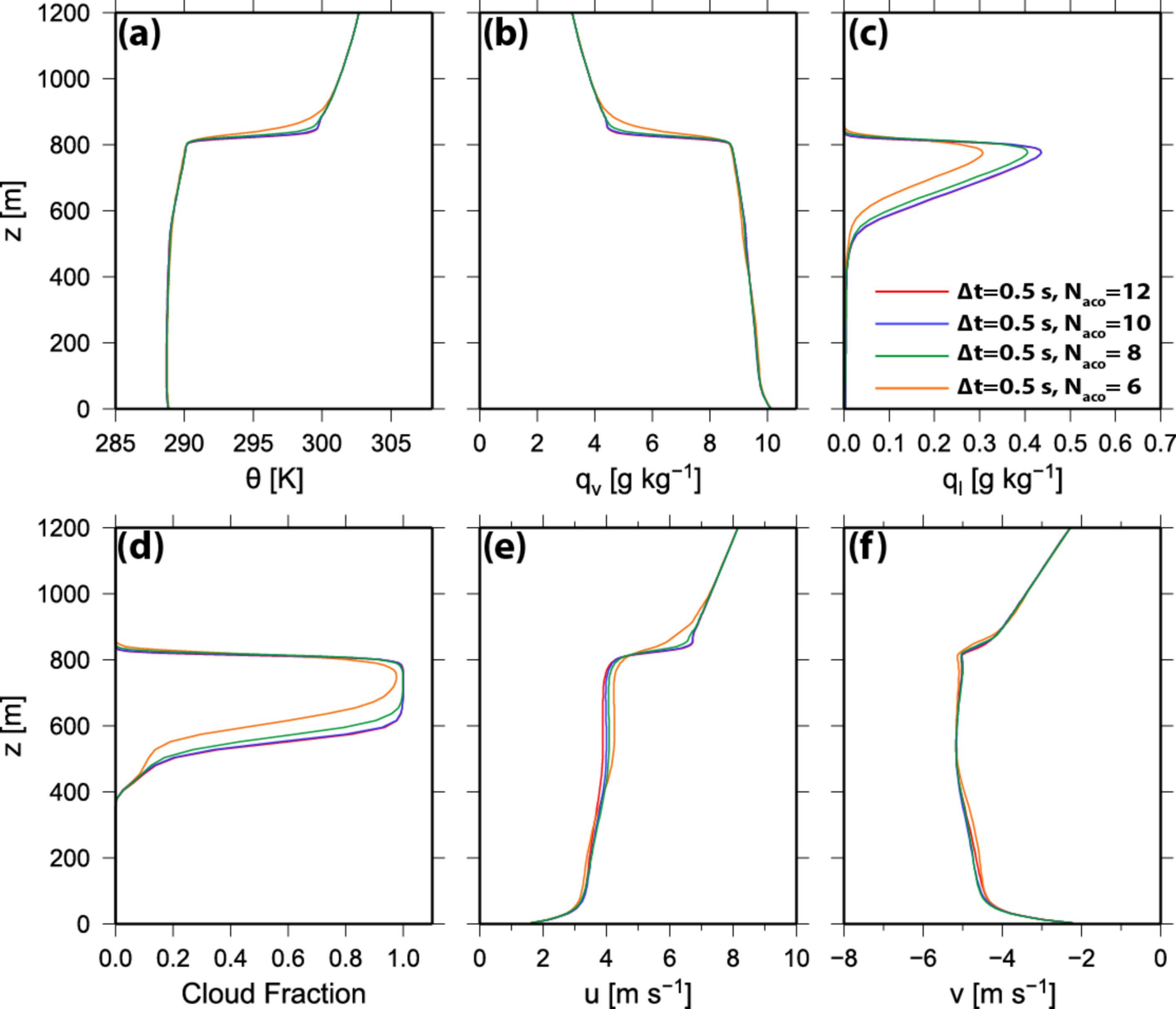


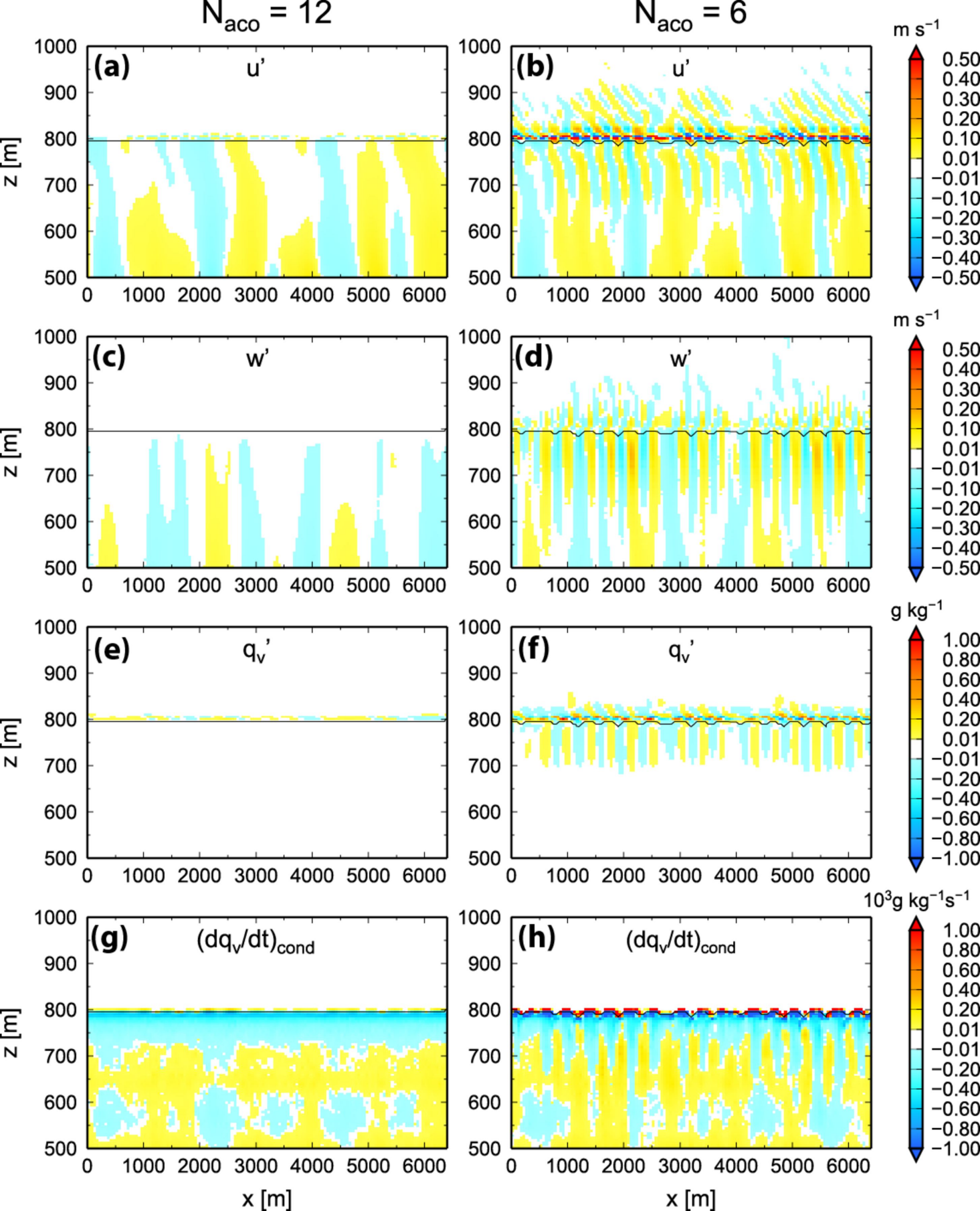
583

584 Figure 12: (a) The LWP (g m^{-2}) and (b) total cloud fraction of the four WRF simulations
 585 with modified dynamical core of the SGP stratocumulus case with different time stepping
 586 choices. MWRRET LWP and TSI cloud fraction observations from the ARM SGP site are
 587 shown for comparison.

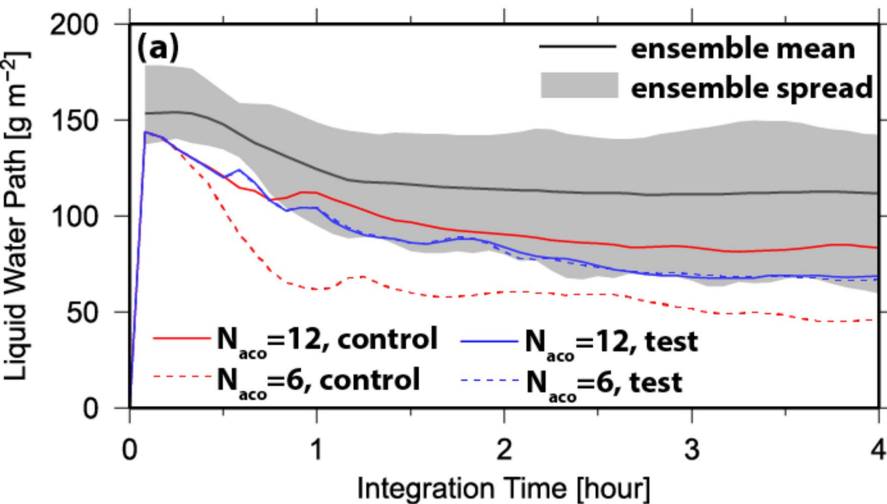




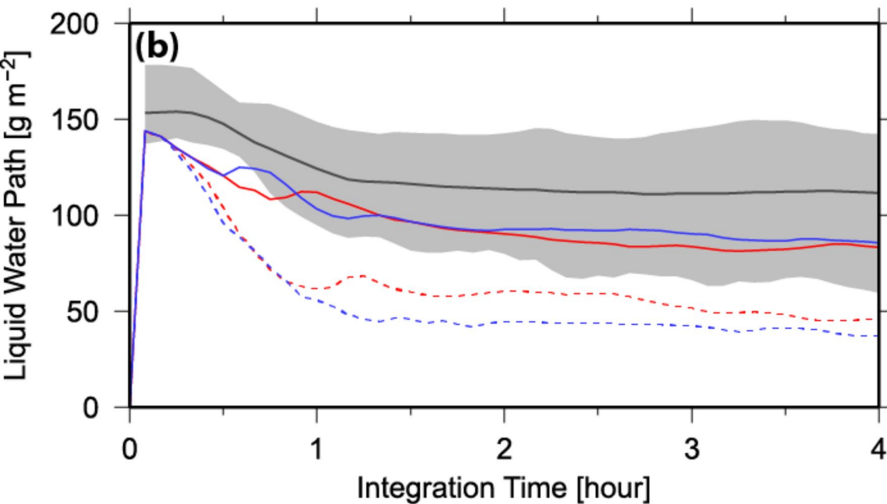




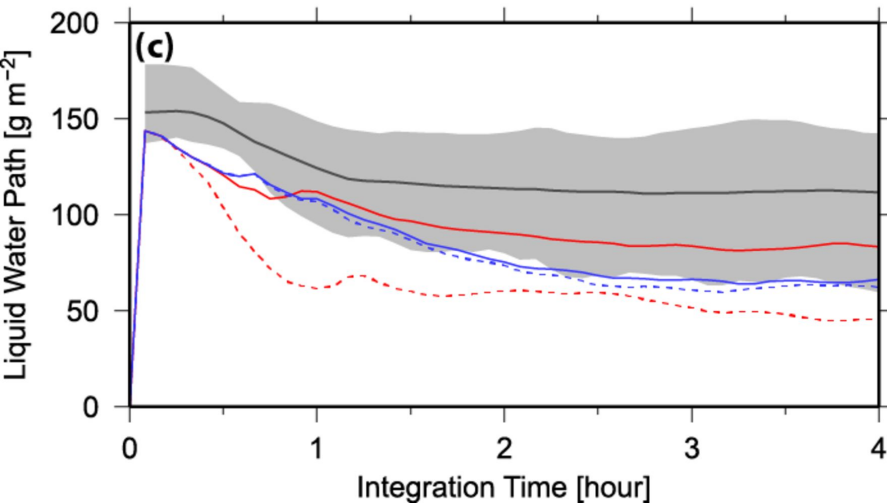
No initial wind



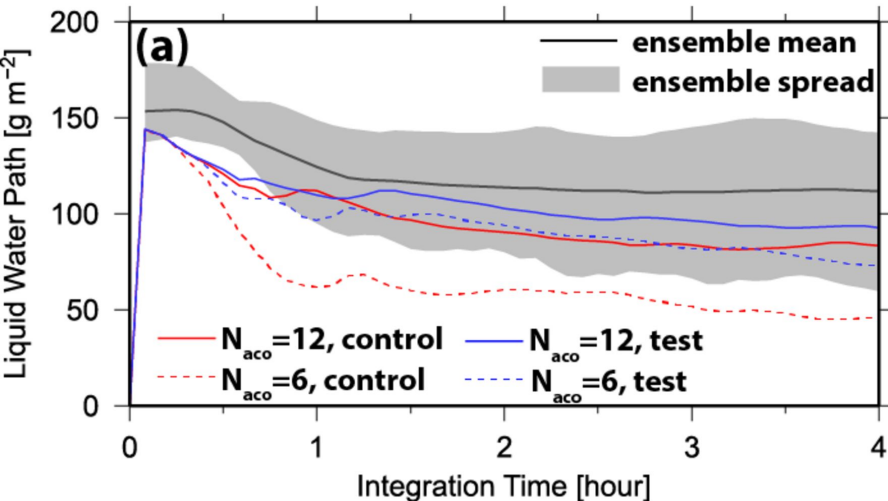
No wind shear



Zero wind speed at inversion



1 g kg⁻¹ smaller Δq_v (2.6 g kg⁻¹)



2 g kg⁻¹ smaller Δq_v (1.6 g kg⁻¹)

